

We are IntechOpen, the world's leading publisher of Open Access books Built by scientists, for scientists

6,900

Open access books available

186,000

International authors and editors

200M

Downloads

Our authors are among the

154

Countries delivered to

TOP 1%

most cited scientists

12.2%

Contributors from top 500 universities



WEB OF SCIENCE™

Selection of our books indexed in the Book Citation Index
in Web of Science™ Core Collection (BKCI)

Interested in publishing with us?
Contact book.department@intechopen.com

Numbers displayed above are based on latest data collected.
For more information visit www.intechopen.com



L-Band SAR Disaster Monitoring for Harbor Facilities Using Interferometric Analysis

Ryo Natsuaki

Abstract

Synthetic aperture radar (SAR) has become a major tool for disaster monitoring. Its all-weather capability enables us to monitor the affected area soon after the event happens. Since the first launch of spaceborne SAR, its amplitude images have been widely used for disaster observations. Nowadays, an accurate orbit control and scheduled frequent observations enable us to perform interferometric analysis of SAR (InSAR) and the use of interferometric coherence. Especially for L-band SAR, its long-lasting temporal coherence is an advantage to perform precise interferometric coherence analysis. In addition, recent high resolution SAR images are found to be useful for observing relatively small targets, e.g., individual buildings and facilities. In this chapter, we present basic theory of SAR observation, interferometric coherence analysis for the disaster monitoring, and its examples for the harbor facilities. In the actual case, DInSAR measurement could measure the subsidence of the quay wall with 3 cm error.

Keywords: synthetic aperture radar (SAR), interferometry, interferometric coherence, disaster monitoring, infrastructure monitoring

1. Introduction

In the last decade, Interferometric Synthetic Aperture Radar (InSAR) has widely spread for measuring ground deformations caused by disasters, for example, earthquakes, volcanic eruptions, or subsidence [1, 2]. It can measure several centimeters of deformation with one pair of SAR images. The accuracy can be increased to several millimeters per year by applying time-series analysis [3, 4]. Compared with traditional optical or amplitude-based SAR analyses, e.g., [5], the advantages of InSAR-based monitoring are, for example, its sensitivity for the deformation and all-weather availability [6–8]. It is effective in the detection of various deformations caused by disasters such as earthquakes [9, 10], volcanic eruptions [11], storms [12], and human disaster [13]. Especially for the long wavelength SAR, i.e., L-band SAR, its long-lasting temporal coherence enables us to perform precise multitemporal interferometric coherence analysis [14]. Polarimetric analysis (PolSAR) has been also proposed for the damage detection using scattering mechanism analysis [15]. In PolSAR mode, SAR transmits both horizontal and vertical polarized waves and receives their co- and cross-polarized signals to see the

scattering mechanism of targets. The collapsed buildings show different scattering mechanisms when they are compared with standing buildings. The most important examples are derived from 2011 off the pacific coast of Tohoku Earthquake [16–19]. Current problem for this method in the operational SARs is that there is less acquisition for full polarimetric mode, narrower swath width, and less spatial resolution caused by the operational limit of the platforms.

Another merit of spaceborne observations is that they have a wider observation swath than that of airborne observations, resulting in faster measurement over a wide area. However, the area of deformation is assumed to be larger than hundreds of meters in the world of InSAR. If its spatial resolution increases, it can be applied to smaller targets' deformation, e.g., the disaster monitoring of harbor facilities smaller than 100 m [20], in addition to the existing change detection methods, e.g., [21, 22].

Currently, operational SAR satellites aim wide swath or high resolution. ALOS-2, COSMO-SkyMed, RADARSAT-2, and TerraSAR/TanDEM-X aim higher resolution (<5 m) with relatively narrow swath width (<50 km), while Sentinel-1 aims wider swath width (200 km) with lower resolution (>20 m). Observation with higher resolution can achieve precise texture of the ground. One can analyze individual buildings with such a high resolution, while preceding researches mostly aim to evaluate in the size of a city block [23, 24]. On the other hand, wider observation swath is required for frequent and scheduled global observation using small number of satellites. That is, the higher frequent acquisition enables us to analyze the region of interest (RoI) without making any conflict with other observation requirements. The frequent observation is a requirement not only for time-series analysis but also for disaster monitoring that the users must observe the affected area as soon as possible. In the next decade, wide swath and high resolution are going to be combined, and the Earth will be observed weekly or bi-weekly with higher than 10 m resolution by SAR satellites such as ALOS-4, NISAR, Sentinel-1 NG, and TanDEM-L.

In such an era, disaster monitoring with SAR data using interferometric analysis becomes more useful [25]. In addition to the traditional amplitude-based change detection, centimeter-order deformation detection and interferometric coherence-based damage assessment will be more operational. One can acquire a delineation map over dozens of square kilometers for the affected area with a few meters resolution several hours after the observation, which cannot be achieved with ground/airborne surveys.

Monitoring harbor facilities plays an important role in the recovery phase in the disaster, because maritime traffic is a backbone of the logistics. For example, a heavy storm may have damaged the seawalls and piers. However, it is difficult to assess the stability of them soon after the event by humans because the ocean is still heavy. A catastrophic earthquake and tsunamis may have damaged a number of harbors simultaneously. In such a case, the authorities have to assess the damage of their facilities and decide whether to rearrange the route. SAR can quickly observe the affected area remotely on behalf of the risky direct observation by humans. This is the reason why SAR can play an important role in the rescue and recovery phase of the disaster. This chapter thinks of it.

In this chapter, we firstly present a fundamental theory for the interferometric analysis of SAR. It includes the basis of differential InSAR (DInSAR) and interferometric coherence analysis. Next, we describe a basic scheme of harbor monitoring for disaster monitoring. Finally, we show several examples in the real case, including the latest L-band SAR satellite Advanced Land Observing Satellite-2 (ALOS-2 or DAICHI-2) [26].

2. Synthetic aperture radar and interferometric analysis

In this section, we briefly explain the system of synthetic aperture radar (SAR) and its interferometric analysis (InSAR), including coherence analysis. Three monitoring methods are shown here. Firstly, wreckages and inundated area detection using amplitude information are described. Next, DInSAR-based displacement detection of the ground is explained. Finally, assessment for the damaged buildings from interferometric coherence is introduced. The descriptions are especially supposed for damage detection in harbor facilities, which is a combination of InSAR and coherence analysis.

2.1 Synthetic aperture radar

The larger antenna diameter derives the higher spatial resolution of radar systems. However, some platforms such as aircraft and satellites cannot deploy a sufficient size of the antenna because of their payload limitations. SAR solves this problem by moving itself and synthesizes the received signals by assuming that the ground targets are fixed [27].

If a SAR can use wide bandwidth, e.g., 1 GHz, it can achieve approximately 0.25 m of spatial resolution in the range direction. A typical high resolution SAR achieves 3–5 m. In the azimuth direction, a pulse repetition frequency (PRF) and aperture length are the large factors. The amplitude of a pixel of SAR image depends on the backscattering coefficient, and the phase depends on the distance between SAR and scatter. The phase information is difficult to handle because the wavelength is too short to measure the ground directly. On the other hand, the phase contains topographic, deformation, and the other valuable information. Those can be analyzed by interferometric analysis.

2.2 Differential interferometric SAR

Figure 1 presents a schematic diagram of InSAR analysis. A SAR image contains amplitude and phase information, in other words, complex-valued information and thus is called Single Look Complex (SLC) image. When we observe the same place from the same orbit multiply and multiply one SLC image (master) and another complex conjugated SLC image (slave), we can make an interferogram. The phase value of the interferogram, φ , is the phase difference between the master and slave. A SAR interferometric phase contains topographic, deformation, ionospheric delay, and tropospheric delay information [28].

In this chapter, we consider that the interferogram, φ , consists of the topographic, φ_{topo} , and deformation, φ_{defo} , components and ignore the others. The topographic component can be estimated by calculating the relationship between the known heights H acquired from a known topographic map as shown in Eq. (1).

$$\varphi_{topo} = \frac{4\pi B_{CT} \cos(\theta - \gamma_{CT})}{\lambda R_m \sin \theta} H \quad (1)$$

where λ is the wavelength of SAR, $B_{CT} \cos(\theta - \gamma_{CT})$ is the perpendicular baseline of the two observations, θ is the incidence angle, and R_m is the slant range distance. Therefore, we can subtract φ_{topo} from the interferogram and measure the deformation component. If deformation occurs between two observations, the deformation phase value, φ_{defo} , corresponds to the shrink or extension in the line-of-sight

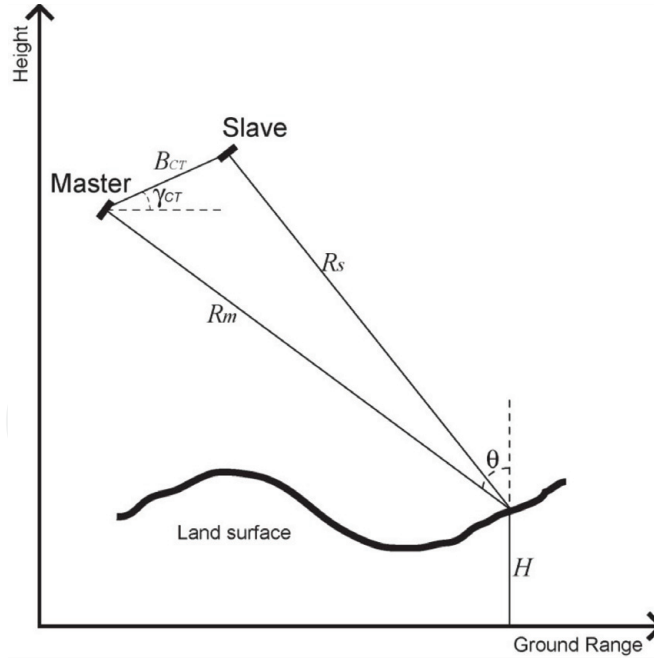


Figure 1.
Schematic diagram of InSAR analysis.

distance between the satellite and ground targets. If we denote the change in the line-of-sight distance as ΔR , the phase value can be calculated with the wave length λ using Eq. (2).

$$\varphi_{defo} = \frac{4\pi}{\lambda} \Delta R \quad (2)$$

As shown in the Eq. (2), the range of phase value is limited between $-\pi$ and π , and thus, we cannot distinguish deformations greater than a quarter wavelength. For example, L-band radar has approximately 24 cm wavelength. When $\Delta R = 0$, $+/-12$, $+/-24...$ cm, φ_{defo} becomes 0 with indefinite $2n\pi$. Therefore, we cannot define the deformation if the neighboring pixels have more than a 6 cm line-of-sight difference. Long wavelength has an advantage to measure a large deformation. We can measure the absolute deformation by unwrapping the phase as long as the deformation satisfies the sampling theorem. The robustness of DInSAR analysis for harbor facilities is discussed in [20]. In [20], it is reported that the average error of the 11 observations was 0.1 cm, and its standard deviation was 0.4 cm for ideal case. That is, there was no systematic error of more than 0.1 cm when we apply the averaging filter when it contains a 0.4 cm variation inside the averaging window. At the same time, the average of the standard deviation of every observation was 1.0 cm. That is, a measured deformation with L-band SAR contains a 1.0 cm error.

2.3 Phase unwrapping

In order to calculate the absolute amount of the deformation, phase unwrapping process is required. The exact operation of phase unwrapping is a line integration of the phase values. We can achieve the integration result, which is independent of the integration path, as long as the amount of deformation between all neighboring pixels satisfies the sampling theorem. If there are residual points, i.e. rotational points, the unwrapping results become dependent on the integration path.

To solve this problem, estimating an appropriate phase value (filtering) and finding a specific integration path is required. Various filtering and unwrapping

methods have been proposed. The Goldstein-Werner filter [29] is the famous low pass filter in the frequency domain. Probability estimation methods such as Markov random field model [30] and Bayesian estimation [31] have been proposed too. Nonlocal filter is widely used for its robustness [32]. Robust unwrapping methods have also been proposed. Branch-cut technique [33] tries to find the minimum cost to cancel the SPs by connecting opposite rotation side ones. Least square methods [34, 35] use Fourier transformation to distinguish steep slope from high frequency noise. The singularity spreading technique [36] is a newly developed method, which simply cancels residues by adding opposite direction to send residue to the other residues. In this chapter, we applied Markov random field model [30] filter and a least-square method [35] for phase unwrapping.

2.4 Interferometric coherence analysis

Interferometric coherence represents the uniformity of the interferometric pair of the SAR images [37, 38]. Interferometric coherence becomes high when the Master and Slave images are close to each other, while it decreases when two are completely different. The coherence value is calculated from the cross-correlation and autocorrelation between the two observations as shown in Eq. (3). When the ground targets are damaged or collapsed by disasters or human activities, the identical position reflects radio waves differently when we compare the pre- and post-event SLCs. In this case, the interferometric phase value contains no information, and the signal in master and slave SLC has no correlation. If the ground surface has been changed by the disaster, this effect appears as a large decrease in interferometric coherence.

$$\gamma = \frac{\langle M^* \bar{S} \rangle}{\sqrt{\langle M^* \bar{M} \rangle} \sqrt{\langle S^* \bar{S} \rangle}}, \quad (3)$$

where M and S represent Master and Slave samples, $M^* \bar{M}$ represents the complex conjugate multiplication of M , and $\langle \rangle$ represents the ensemble average of the samples in $\langle \rangle$. In short, γ is a normalized cross-correlation of M and S , and thus, it varies from 0 to 1. $\gamma = 1$ only happens when $M = S$ and $\gamma = 0$ never occurs because of randomness. A large facility has a relatively high (approximately 0.7–0.9) value. Contrarily, bare soil and concrete caissons have low ($0.3 <$) values because they have smooth surface and low reflectivity in radar. An insufficient window size will overestimate the coherence value, while the larger window size will reduce the ground resolution. The window size of the ensemble average in Eq. (3) is 5×5 pixels in this chapter. The interferometric coherence largely depends on the surface roughness and temporal stability. If it is too smooth and/or unstable, such as water surface, concrete surface, and highly active region, the radio wave does not return to the satellite coherently.

Coherence γ also depends on the interval of M and S . Though it is stable, the ground surface changes time by time. If master and slave images are acquired in, for example, different years, γ becomes lower. This is called temporal decorrelation. To avoid this effect, it is required to observe the same place frequently. In general, a lower band SAR has a slower temporal decorrelation.

When we compare γ of two interferograms, we can detect the effect of disasters. This is called multitemporal coherence analysis; its aim is to detect the damaged part from the change in γ . If we have at least one interferogram prior to the disaster, a pre-event interferogram and an interferogram which is made from pre-event and post-event SLCs, a co-event interferogram, we can compare their coherence values.

This is called multitemporal interferometric coherence change detection. If the co-event interferometric coherence is lower than the pre-event one, though considering temporal decorrelation, it can be regarded that scatterers on the surface have been damaged and/or moved largely. Two definitions for the coherence decrease $d\gamma$ can be considerable. One is the simple difference or un-normalized coherence decrease (CD) $d\gamma_{un}$, and the other is the normalized coherence decrease $d\gamma_{norm}$, as shown in Eqs. (4) and (5).

$$d\gamma_{un} = \gamma_{pre} - \gamma_{co} \quad (4)$$

$$d\gamma_{norm} = \frac{\gamma_{pre} - \gamma_{co}}{\gamma_{pre} + \gamma_{co}} \quad (5)$$

where the pre-event coherence is γ_{pre} and the co-event coherence is γ_{co} . Eq. (4) requires relatively large γ_{pre} and cannot be applied for low coherency areas, such as vegetated ground. On the other hand, Eq. (5) does not require large γ_{pre} , while the temporal decorrelation will suffer in accuracy. In this chapter, Eq. (4) is applied because harbor facilities generally have large γ_{pre} in long temporal baseline.

The facilities should be regarded as damaged when $d\gamma_{un}$ exceeds the specific threshold. The threshold is generally defined manually to reduce the effect of temporal and spatial decorrelations. In [39], the authors found that the buildings which are larger than 200m² can be evaluated by setting the threshold 0.3. When the buildings exceed the threshold, they were moderately or severely damaged when they are classified by EMS-98 scheme [40]. In this chapter, therefore, threshold for $d\gamma_{un}$ is set to 0.3.

2.5 Scattering mechanisms of harbor facilities

In order to apply those analyses above to the disaster monitoring of harbor facilities, the scattering mechanisms of SAR are briefly described. Numerical models are the same to the other cases; however, it is worth mentioning what the scatterers are in the harbor. **Figure 2** shows the schematic image of harbor. In the figure, SAR satellite is observing the harbor from left top of the figure.

Figure 2(a) shows the scattering mechanisms in normal condition. Region A is water, and therefore, backscattering coefficient is very low. Region B is the bare ground, and its brightness depends on its roughness. If the ground is covered by concrete or asphalt, it can be seen dark as same as water. Region C is layover of the facilities, and its surface scattering from the roof can be seen. On the other hand, Region D is a shadow region and Point Z cannot be observed by the satellite. Water, ground, and vertical walls work as smooth surface, and therefore, double-bounce effects are seen in Point X and Y.

Figure 3 presents an example of airborne L-band SAR image and the corresponding spaceborne optical image of the harbor. There are multiple bright targets which exist at the edge of the pier and the buildings. Those are the double-bounce effects. On the other hand, the top of the pier which is covered by asphalt and concrete is mostly dark as the water. The brightness of the rooftop of buildings depends on the structure of them. Those bright scatterers which do not move between two observations have high coherence. Note that ships have no coherence because they move on the water. Other moving facilities such as cars, containers, and cranes do not have high coherence too. On the other hand, stable facilities, e.g., buildings, walls, and vegetation have high coherence in L-band SAR. In short, interferometric analysis is applicable only to the stable bright scatterers.

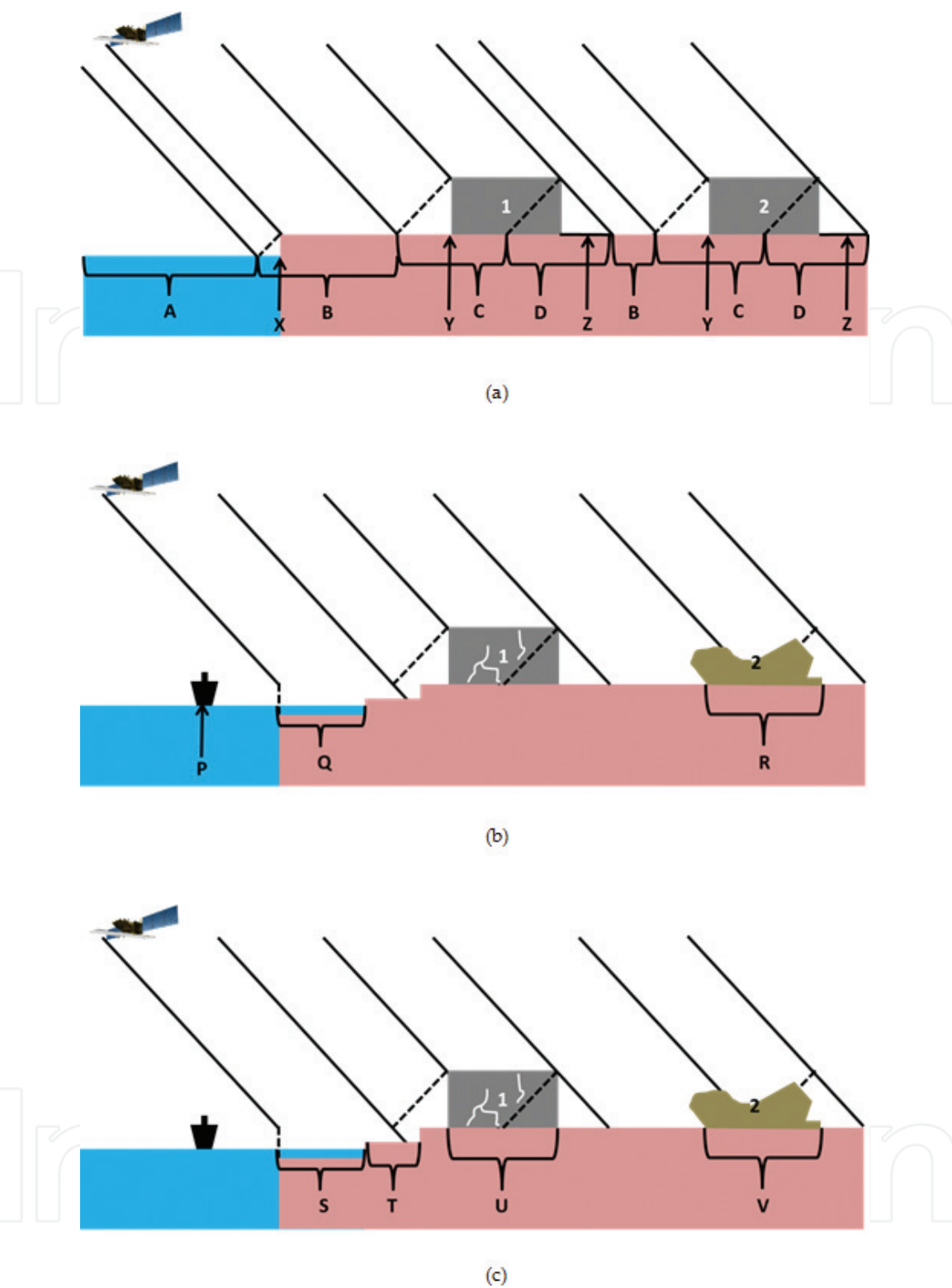
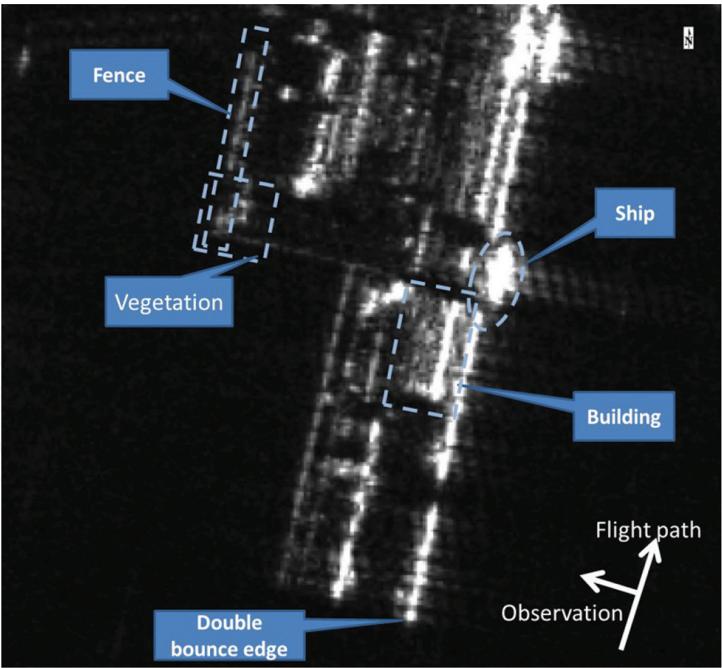


Figure 2. Schematic image for disaster monitoring of harbor facilities using SAR. (a) Scattering mechanism in harbor and change detection based on (b) amplitude and (c) interferometric analysis.

Figure 2(b) shows a schematic diagram of the traditional amplitude-based SAR analysis. By comparing the pre- and post-disaster observation, the followings can be found. Object P wreckages on the water reflects the radar signal and appears in the post-disaster image. Region Q, an inundated area, will decrease the backscattering coefficients, and therefore, it appears as water region in the postdisaster image. Roads and other smooth surfaces are originally dark in SAR image and therefore may not change the amplitude by flooding. In addition, insufficient amount of subsidence or deformation will not be detected from amplitude image. Region R,



(a)



(b)

Figure 3.
Example of (a) SAR and (b) optical observation among harbor facilities.

the totally collapsed buildings, can be seen as a brighter scatterer in the postdisaster image, because in general, demolished buildings are more random surface than standing ones. On the other hand, slightly damaged buildings do not show any significant change in the amplitude image. In short, amplitude-based analysis can detect significant difference of the scatterers.

Figure 2(c) shows what can be observed by interferometric analysis. As water and surface has no coherency, wreckages on the water are not visible by interferometric analysis. Inundated Region S shows significant drop of coherence. Region T, deformation of the ground including subsidence or lateral flow, can be seen by interferometric phase and can be measured how large the surface moved. To calculate the absolute amount of the deformation, it requires relatively high coherence,

that is, the place where the deformation can be measured has less damage. Region U and V, moderately damaged and collapsed buildings, can be detected by interferometric coherence analysis too. Its sensitivity is discussed precisely in [39].

In summary, some damages can be detected only by amplitude information, while the others can be detected only by interferometric analysis. Precise centimeter-order deformation can be measured when the surface keeps enough coherencies.

In a qualitative manner, one can segmentalize the disaster affected harbor facilities as following features.

- Nonaffected area can be recognized as high coherence and same amplitude areas.
- Deformation can be measured by DInSAR as long as the surface keeps enough coherence. Note that the phase component of the interferogram is relative value in the line-of-sight direction and not the absolute deformation of neither vertical nor horizontal direction.
- Moderately damaged buildings can be found by the decrease of coherence.
- Severely damaged buildings can be found by both decrease of coherence and increase of amplitude.
- Inundated areas appear as significant drop of amplitude as well as decrease of coherence.
- Wreckages on the water can be found from increase of the amplitude in the water region.

3. Damage detection scheme

Here, a brief detection scheme is introduced. In the rescue and recovery phase of disaster, mapping an affected area is one of the urgent tasks. The authorities use the delineation map for planning their activities. However, not all the responsible persons are familiar with remote sensing, especially for SAR. Therefore, intuitive classification is required.

Figure 4 shows an example of the classification flow. The classification scheme consists of five processes. First, the region which amplitude dropped more than 6 dB than pre-disaster data or weaker than the known water region is regarded as under the water and indicated as blue on map. The area which was affected by subsidence, tidal wave, and/or tsunami will be visualized.

-
- 1. Amp. of Pre - Post > 6dB (amp. drop)
 - 2. Amp. of Pre - Post < -6dB (amp. increase)
 - 3. $\gamma_{pre} - \gamma_{co} > 0.3$ (Coh. drop)
 - 4. $\gamma_{co} > 0.6$ (High Coh.)
 - 5. If 4. and 5. conflict, make it blank

Figure 4.
Decision flow of the quick assessment.

Second, the region in which amplitude increased more than 6 dB than pre-disaster data is indicated as yellow on map. Wreckages and totally collapsed buildings will appear here.

Third, the region which coherence dropped more than 0.3 than pre-disaster dataset is regarded as inundated and indicated as red on map. Moderately or severely damaged facilities will be shown in this color. Totally collapsed buildings will be also classified here too.

Fourth, the region in which coherence is higher than 0.6 is regarded as not affected and indicated as green. Showing “safe zone” is demanded for the authorities to decide from where they start their operations.

If the region fulfills both 3 and 4, they do indicate none of them. Some large buildings have higher than 0.9 of coherence in pre-disaster pair, and their coherence may keep higher than 0.6 in co-disaster pair. In such a case, it is difficult to distinguish whether the buildings are damaged or not.

Measurement results for the deformation by DInSAR are presented in the different layer.

4. Examples

In this section, we applied the classification scheme to two examples. First is Ishinomaki port, Japan, which was severely affected by the 2011 off the Pacific coast of Tohoku earthquake. The port was observed by ALOS that was operated by JAXA until 2011. The second example is Kumamoto port, Japan, which was slightly affected by 2016 Kumamoto earthquake and observed by the latest ALOS-2. Note that the scheme can be applied to the other disasters such as typhoon and is evaluated in [20].

In Kumamoto port case, we measured the lateral flow with DInSAR. As the area is enough small, we assumed that all phase components consist of topography and deformation and ignored other phase components in the interferogram, such as the ionospheric [41–43] and tropospheric [44, 45] delays.

4.1 Ishinomaki port, Japan in 2011 off the Pacific coast of Tohoku earthquake

Ishinomaki port, Miyagi prefecture, Japan, was severely affected by the 2011 off the Pacific coast of Tohoku earthquake on March 11, 2011. A large tsunami hits the port, and almost all facilities were collapsed, damaged, or flushed out. The affected area was observed by ALOS several times. Here, we use the data set of Path 402, Frame 760. The observation dates are April 1, 2011, August 14, 2010, and May 14, 2010. The first two are used for co-event pair, and the latter two are for pre-event pair. Thanks to the L-band SAR's long lasting coherence, 8 months interval pair can be used effectively for the analysis. ALOS has approximately 10 m by 5 m resolution and therefore hardly investigate an identical building in general. However, the harbor facilities in this port were enough large to be distinguished. On the other hand, the deformation itself was too large to be measured by DInSAR. Therefore, we present a delineation map only.

Figure 5 presents the damage assessment results for the Ishinomaki port. As shown in the figure, most part of the coast line of the city was colored in red; the buildings are detected as moderately or severely damaged. In the left side of the figure, there is a large inundated area which is colored in blue. From **Figure 5**, it is also clear that some buildings on the hills in the north part of the city survived from the earthquake and tsunami.

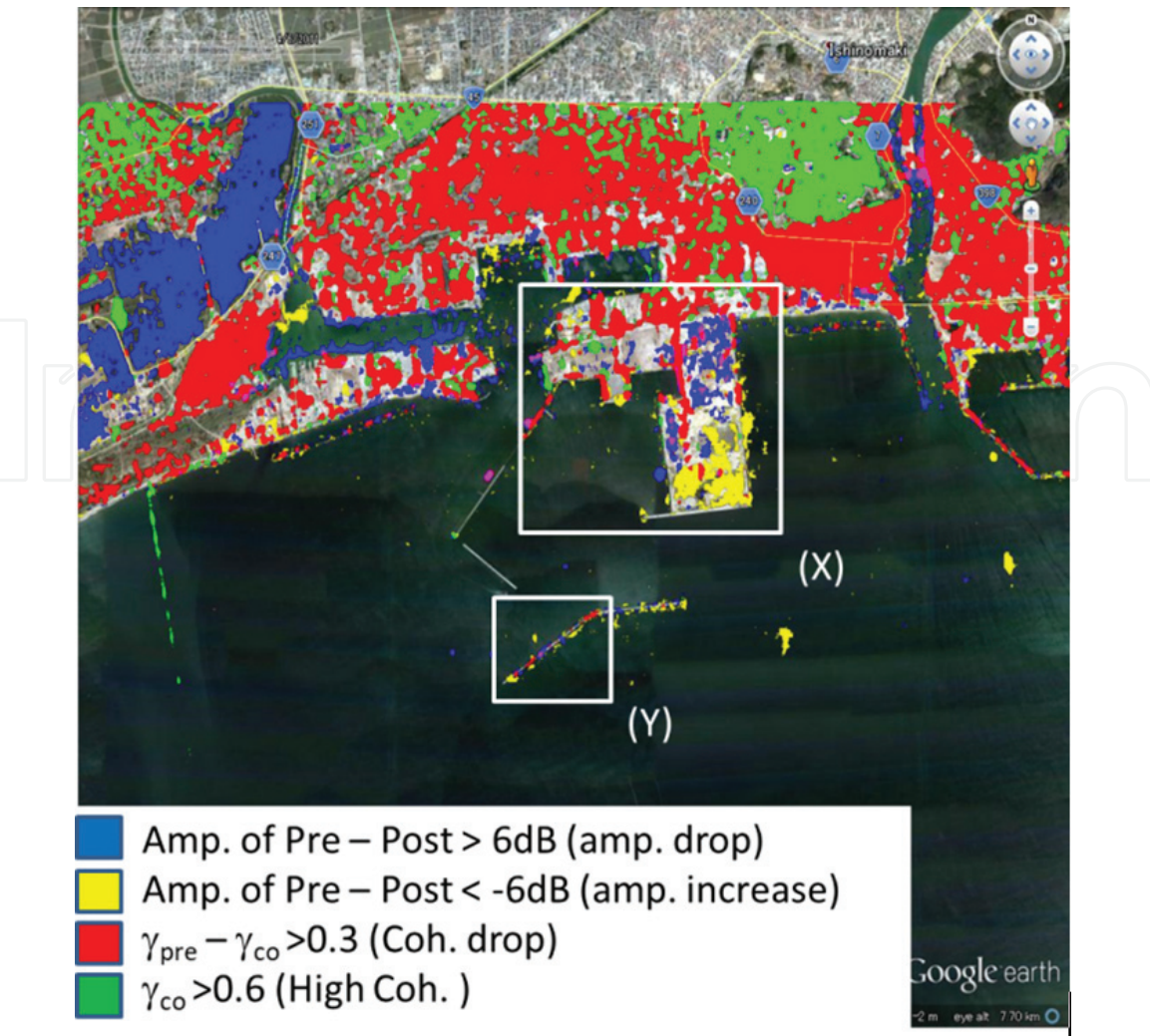


Figure 5.
Damage assessment results for Ishinomaki port, Japan, in 2011 off the Pacific coast of Tohoku earthquake.

Figure 6 shows the closed-up images with optical data of white rectangles, which are marked as X and Y in **Figure 5**. **Figure 6(a)** is a closed-up image for the piers and its comparison in optical images in Region X. Most facilities are demolished, while some of them are remaining. The pier in right hand side has both inundated and wreckage-covered area.

Figure 6(b) is a closed-up image and its optical comparison for the Region Y in **Figure 5**. This part is a breakwater of the port. Soon after the disaster, it is sometimes difficult to approach the offshore facilities. On the other hand, satellite-based SAR can observe them. In this case, tsunami hits the breakwater and some of them are sunk under the water. Wreckages are also found surrounding them. Most damaged buildings were found by interferometric coherence analysis. This is probably caused by the orientation, size, and structure of the buildings.

4.2 Kumamoto port, Japan in 2016 Kumamoto earthquake

Kumamoto port, Kumamoto prefecture, Japan, was hit by the earthquake on April 15, 2016. ALOS-2 had observed the port half a day before the earthquake and observed there again in the next revisit cycle (14-days) on April 29, 2016. There is another observation record from the same orbit on November 14, 2014, and therefore, we can perform the interferometric coherence analysis. The path and frame number of the observation are Path 28 and Frame 2930, respectively.

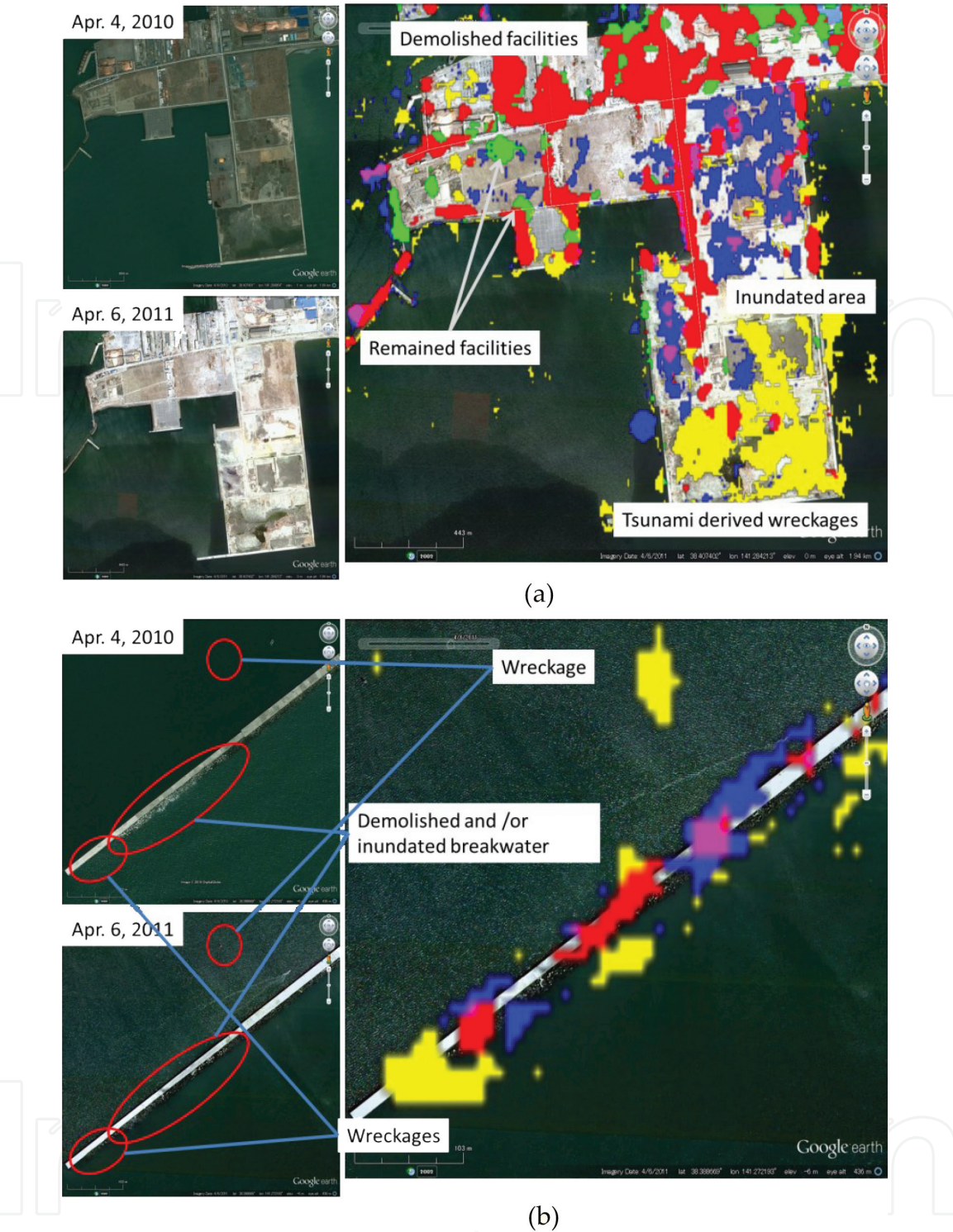


Figure 6.
Close up images for **Figure 5**: (a) Region X and (b) Region Y.

Figure 7 shows an example of the interferometric phase and the position of the port. Each fringe of the interferometric phase represents 12 cm deformation. Fortunately, the port is enough far from the epicenter. Its overall deformation was small enough to continue the operation. **Figure 8** presents the delineation map and the analytical results for coherence analysis and DInSAR measurement. **Figure 8(a)** shows the delineation map. Fortunately, most part of the pier received no damage. Therefore, we could only detect the difference of the

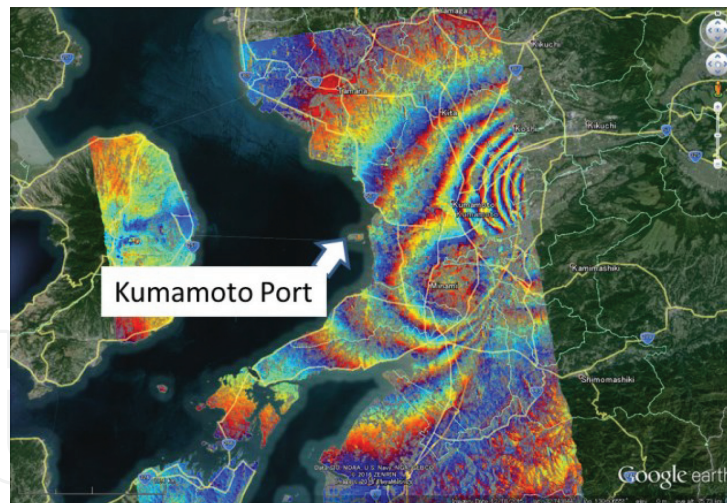


Figure 7.
Interferogram in Kumamoto earthquake.

berthing ships between April 15 and 29. There were almost no damaged facilities, and therefore, it is hardly visible to see nongreen part. In **Figure 8(b)**, we show the coherence drop data, red color in **Figure 8(a)**. Now, it is visible that the right hand side of the pier has several damaged facilities. According to the rapid report from the port [46], some roads and facilities received several damages.

In this case, temporal baseline of γ_{pre} is almost 17 months. In such a long interval, a SAR, which uses higher frequency (e. g., X- or C-band), cannot achieve enough coherence to compare with γ_{co} . These results indicate that L-band SAR may observe the earth from additional incidence angle once in a several years in order to prepare for the disaster. If we have multiple archives from multiple incidence angles, the operator can move the satellite to observe the affected area as soon as possible and compare the observation results with the archives. Such operation will greatly help the corresponding authorities because they need not to wait for the next “scheduled” observation.

Kumamoto port had been under construction to landfill. A lateral flow occurred in the north part of the pier. **Figure 8(c)** shows the measurement results of the DInSAR. The unwrapped result shows more than 20 cm of line-of-sight displacement. As ALOS-2 observed the port from west of the port, west half of the port moved toward the satellite and the east half moved away from the satellite. On the other hand, the existing parts show only small deformations. For example, the quay wall showed 5–10 cm subsidence by DInSAR measurement. On the other hand, the actual measurement in [46] was 7 cm. Therefore, the error in this case was 3 cm, which is larger than the ideal case in [20] (1 cm). This is caused by, for example, filtering errors, unwrapping errors, or the randomness in the subsidence. In summary, DInSAR could measure the subsidence of the quay wall with several centimeter of error. The measured deformation can be used in the recovery phase of the disaster. As single DInSAR pair can measure the line-of-sight displacement, three dimensional measurements require more than three observations. Especially for the satellite SAR, it is difficult to measure north-south deformation by interferometric analysis because it usually flights polar orbit and can only observe from east or west. If the deformation is enough large to be detected by co-registration, pixel-offset method can be applied.

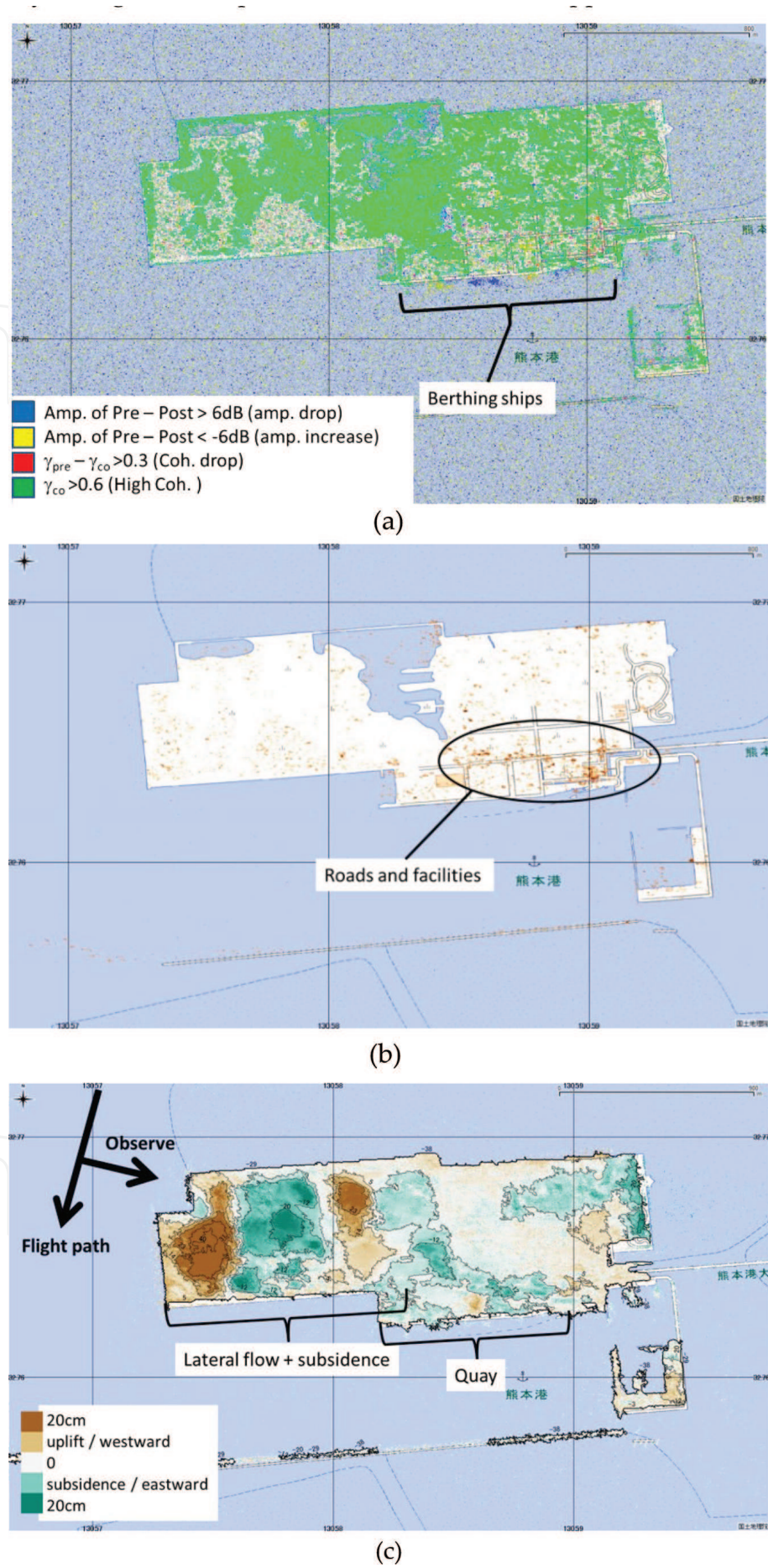


Figure 8. Damage assessment results for Kumamoto port, Japan, in 2016 Kumamoto earthquake. (a) Damage assessment map, (b) coherence dropped part only, and (c) deformation map.

5. Conclusion

In this chapter, a rapid damage assessment scheme which is based on SAR interferometric analysis was introduced. With a combination of amplitude analysis, it is able to show an easy-understanding and enough-accurate delineation map. Furthermore, interferometric analysis can provide centimeter-order deformation map. In the example case of Kumamoto earthquake, ALOS-2 detected 5–10 cm subsidence in the quay wall, which was 7 cm in real measurement. These results are highly appreciated by the disaster corresponding authorities. In this chapter, a basic theory is shown. Its accuracy can be easily improved by, for example, machine learning and data-fusions with the other observations.

Acknowledgements

The ALOS/ALOS-2 original data are copyrighted by MEXT and JAXA, and provided under JAXA 6th ALOS Research Announcement PI No. 3044. The experiments were partially supported by the Council for Science, Technology, and Innovation, “Cross-ministerial Strategic Innovation Promotion Program (SIP), Infrastructure Maintenance, Renovation, and Management” (funding agency: NEDO). The maps in this chapter are provided from Geospatial Information Authority under the Ministry of Land, Infrastructure, Transport and Tourism of Japan. Google Inc. provided the aerial images on Google Earth. Dr. Natsuaki is currently with German Aerospace Center as a visiting scientist sponsored by JSPS Overseas Research Fellowships.

Conflict of interest


The author declares no conflict of interest.

Author details

Ryo Natsuaki
Department of Electrical Engineering and Information Systems, The University of Tokyo, Tokyo, Japan

*Address all correspondence to: natsuaki@eis.t.u-tokyo.ac.jp

IntechOpen

© 2018 The Author(s). Licensee IntechOpen. This chapter is distributed under the terms of the Creative Commons Attribution License (<http://creativecommons.org/licenses/by/3.0>), which permits unrestricted use, distribution, and reproduction in any medium, provided the original work is properly cited. 

References

- [1] Boerner WM. Recent advances in extra-wide-band polarimetry, interferometry and polarimetric interferometry in synthetic aperture remote sensing and its applications, radar, sonar navigation. IEE Proceedings. 2003;**150**(3):113-124
- [2] Plank S. Rapid damage assessment by means of multi-temporal SAR - a comprehensive review and outlook to Sentinel-1. Remote Sensing. 2014;**6**(6): 4870-4906. DOI: 10.3390/rs6064870
- [3] Ferretti A, Prati C, Rocca F. Permanent scatterers in SAR interferometry. IEEE Transactions on Geoscience and Remote Sensing. 2001; **39**(1):8-20
- [4] Ferretti A, Fumagalli A, Novati F, Prati C, Rocca F, Rucci A. A new algorithm for processing interferometric data-stacks: SqueeSAR. IEEE Transactions on Geoscience and Remote Sensing. 2011;**49**(9):3460-3470
- [5] Liu W, Yamazaki F, Adriano B, Mas E, Koshimura S. Development of building height data in Peru from high-resolution SAR imagery. Journal of Disaster Research. 2014;**9**(6): 1042-1049. DOI: 10.20965/jdr.2014.p1042
- [6] Matsuoka M, Yamazaki F. Building damage mapping of the 2003 Bam, Iran, earthquake using ENVISAT/ASAR intensity imagery. Earthquake Spectra. 2005;**21**(S1):S285-S294
- [7] Fielding EJ. Surface ruptures and building damage of the 2003 Bam, Iran, earthquake mapped by satellite synthetic aperture radar interferometric correlation. Journal of Geophysical Research. 2005;**110**(B03302)
- [8] Arciniegas GA, Bijker W, Kerle N, Tolpekin VA. Coherence- and amplitude-based analysis of seismic damage in Bam, Iran, using ENVISAT ASAR data. IEEE Transactions on Geoscience and Remote Sensing. 2007; **45**(6):1571-1581
- [9] Natsuaki R, Nagai H, Motohka T, Ohki M, Watanabe M, Thapa RB, et al. SAR interferometry using ALOS-2 PALSAR-2 data for the Mw 7.8 Gorkha Nepal earthquake, Earth, Planets and Space. 2016;**68-15**:1-13. DOI: 10.1186/s40623-016-0394-4
- [10] Jimenez C, Moggiano N, Mas E, Adriano B, Koshimura S, Fujii Y, et al. Seismic source of 1746 Callao earthquake from tsunami numerical Modeling. Journal of Disaster Research. 2013;**8**(2):266-273. DOI: 10.20965/jdr.2013.p0266
- [11] Hooper A, Sigmundsson F, Prata F. Remote sensing of volcanic hazards and their precursors. Proceedings of the IEEE. 2012;**100**(10):2908-2930
- [12] Nakmuenwai P, Yamazaki F, Liu W. Multi-temporal correlation method for damage assessment of buildings from high-resolution SAR images of the 2013 typhoon Haiyan. Journal of Disaster Research. 2016;**11**(3):577-592. DOI: 10.20965/jdr.2016.p0577
- [13] Liu W, Yamazaki F, Sasagawa T. Monitoring of the recovery process of the Fukushima Daiichi nuclear power plant from VHR SAR images. Journal of Disaster Research. 2016;**11**(2):236-245. DOI: 10.20965/jdr.2016.p0236
- [14] Wei M, Sandwell DT. Decorrelation of L-band and C-band interferometry over vegetated areas in California. IEEE Transactions on Geoscience and Remote Sensing. 2010;**48**(7):2942-2952
- [15] Yamaguchi Y. Disaster monitoring by fully polarimetric SAR data acquired with ALOS-PALSAR. Proceedings of the IEEE. 2012;**100**(10):2851-2860

- [16] Sato M, Chen SW, Satake M. Polarimetric SAR analysis of tsunami damage following the march 11, 2011 East Japan earthquake. *Proceedings of the IEEE*. 2012;**100**(10):2861-2875
- [17] Watanabe M, Motohka T, Miyagi Y, Yonezawa C, Shimada M. Analysis of urban areas affected by the 2011 off the pacific coast of Tohoku earthquake and tsunami with L-band SAR full-polarimetric mode. *IEEE Geoscience and Remote Sensing Letters*. 2012;**9**(3): 472-476
- [18] Chen SW, Sato M. Tsunami damage investigation of built-up areas using multitemporal spaceborne full polarimetric SAR images. *IEEE Transactions on Geoscience and Remote Sensing*. 2013;**51**(4):1985-1997
- [19] Chen SW, Wang XS, Sato M. Urban damage level mapping based on scattering mechanism investigation using fully polarimetric SAR data for the 3.11 East Japan earthquake. *IEEE Transactions on Geoscience and Remote Sensing*. 2016;**54**(12): 6919-6929
- [20] Natsuaki R, Anahara T, Kotoura T, Iwatsuka Y, Tomii N, Katayama H, et al. Synthetic aperture radar interferometry for disaster monitoring of harbor facilities. *Journal of Disaster Research*. 2017;**12**(3):526-535
- [21] Matsuoka M, Estrada M. Development of earthquake-induced building damage estimation model based on ALOS/PALSAR observing the 2007 Peru earthquake. *Journal of Disaster Research*. 2013;**8**(2):346-355. DOI: 10.20965/jdr.2013.p0346
- [22] Adriano B, Mas E, Koshimura S, Estrada M, Jimenez C. Scenarios of earthquake and tsunami damage probability in Callao region, Peru using tsunami fragility functions. *Journal of Disaster Research*. 2014;**9**(6):968-975. DOI: 10.20965/jdr.2014.p0968
- [23] Yonezawa C, Takeuchi S. Decorrelation of SAR data by urban damages caused by the 1995 Hyogokennanbu earthquake. *International Journal of Remote Sensing*. 2001;**22**:1585-1600
- [24] Matsuoka M, Nojima N. Building damage estimation by integration of seismic intensity information and satellite L-band SAR imagery. *Remote Sensing*. 2010;**2**(9): 2111-2126
- [25] Milillo P, Riel B, Minchew B, Yun SH, Simons M, Lundgren P. On the synergistic use of SAR constellations' data exploitation for earth science and natural hazard response. *IEEE Journal of Selected Topics in Applied Earth Observations and Remote Sensing*. 2016;**9**(3):1095-1100
- [26] Arikawa Y, Saruwatari H, Hatooka Y, Suzuki S. PALSAR-2 launch and early orbit operation result. *International Geoscience and Remote Sensing Symposium (IGARSS)*. 2014;**2014**: 3406-3409
- [27] Cumming IG, Wong FHC. *Digital Processing of Synthetic Aperture Radar Data: Algorithms and Implementation*. Norwood, MA, USA: Artech House; 2005
- [28] Ghiglia DC, Pritt MD. *Two-Dimensional Phase Unwrapping: Theory, Algorithms, and Software*. John Wiley & Sons, Inc.; 1998:31-58
- [29] Goldstein RM, Werner CM. Radar interferogram filtering for geophysical applications. *Geophysical Research Letters*. 1998;**25**(21):4035-4038
- [30] Yamaki R, Hirose A. Singular unit restoration in interferograms based on complex-valued Markov random field model for phase unwrapping. *IEEE Geoscience and Remote Sensing Letters*. 2009;**6**(1):18-22

- [31] Ferraiuolo G, Poggi G. A Bayesian filtering technique for SAR interferometric phase fields. *IEEE Transactions on Image Processing*. 2004;**13**(10):1368-1378
- [32] Sica F, Cozzolino D, Zhu XX, Verdoliva L, Poggi G. InSAR-BM3D: A nonlocal filter for SAR Interferometric phase restoration. *IEEE Transactions on Geoscience and Remote Sensing*. 2018; **56**:3456-3467
- [33] Costantini M. A novel phase unwrapping method based on network programming. *IEEE Transactions on Geoscience and Remote Sensing*. 1998; **36**(3):813-821
- [34] Pritt MD, Shipman JS. Least-squares two-dimensional phase unwrapping using FFT's. *IEEE Transactions on Geoscience and Remote Sensing*. 1994; **32**(3):706-708
- [35] Suksmono AB, Hirose A. Progressive transform-based phase unwrapping utilizing a recursive structure. *IEICE Transactions on Communications*. 2006;**E89-B**(3): 929-936
- [36] Yamaki R, Hirose A. Singularity-spreading phase unwrapping. *IEEE Transactions on Geoscience and Remote Sensing*. 2007;**45**(10):3240-3251
- [37] Touzi R, Lopes A, Bruniquel J, Vachon PW. Coherence estimation for SAR imagery. *IEEE Transactions on Geoscience and Remote Sensing*. 1999; **37**(1):135-149. DOI: 10.1109/36.739146
- [38] Abdelfattah R, Nicolas JM. Interferometric SAR coherence magnitude estimation using second kind statistics. *IEEE Transactions on Geoscience and Remote Sensing*. 2003; **44**(2):1942-1953
- [39] Natsuaki R, Nagai H, Tomii N, Tadono T. Sensitivity and limitation in damage detection for individual buildings using InSAR coherence - a case study in 2016 Kumamoto earthquakes. *Remote Sensing*. 2018; **10**(2):245
- [40] Grunthal G, editor. *European Macroseismic Scale 1998*. Luxembourg: Centre Europeen de Geodynamique et de Seismologie; 1998
- [41] Mayer F, Bamler N, Jakowski R, Fritz T. The potential of low-frequency SAR systems for mapping ionospheric TEC distributions. *IEEE Geoscience and Remote Sensing Letters*. 2006;**3**(4): 560-564
- [42] Gomba G, Parizzi A, De Zan F, Eineder M, Bamler R. Toward operational compensation of ionospheric effects in SAR interferograms: The split-spectrum method. *IEEE Transactions on Geoscience and Remote Sensing*. 2015; **54**(3):1446-1461. DOI: 10.1109/TGRS.2015.2481079
- [43] Jung HS, Lee WJ. An improvement of ionospheric phase correction by multiple-aperture interferometry. *IEEE Transactions on Geoscience and Remote Sensing*. 2015;**53**(9):4952-4960
- [44] Doin MP, Lasserre C, Peltzer G, Cavalié O, Doubre C. Corrections of stratified tropospheric delays in SAR interferometry: Validation with global atmospheric models. *Journal of Applied Geophysics*. 2009;**69**:35-50. DOI: 10.1016/j.jappgeo.2009.03.010
- [45] Bekaert DPS, Walters RJ, Wright TJ, Hooper AJ, Parker DJ. Statistical comparison of InSAR tropospheric correction techniques. *Remote Sensing of Environment*. 2015;**170**:40-47. DOI: 10.1016/j.rse.2015.08.035
- [46] Nodu A. Damage Reports of Ports and Airports, Rapid Communication for 2016 Kumamoto Earthquake, Earthquake Engineering Committee, Japan Society of Civil Engineering. Available from <http://committees.jsce.or.jp/eec2/node/76> [in Japanese, Accessed: 2018-08-31]